Novel High-Performance Grid Fins for Missile Control at High Speeds: Preliminary Numerical and Experimental Investigations

Erich Schülein
DLR, Institut für Aerodynamik
und Strömungstechnik
Bunsenstr. 10, 37073 Göttingen
GERMANY

erich.schuelein@dlr.de

Daniel Guyot
currently: TU Berlin, Institut für
Strömungsmechanik und Technische Akustik
Müller-Breslau-Str. 8, 10623 Berlin
GERMANY

daniel.guyot@tu-berlin.de

ABSTRACT

The object of this work is the investigation of new locally swept grid fins (lattice wings) regarding its potential of the performance improvement at high speeds. Detailed examinations include numerical simulations of the supersonic flow around the conventional and locally swept planar and lattice wings of infinite span as well as direct force measurements at corresponding realistic finite span models in the Ludwieg Tube Facility at DLR (RWG). The investigations were performed at free-stream Mach numbers from 2 to 6 for angles of attack varied from 0 to 10 degrees. The performance of the lattice wings was assessed on the basis of the zero-lift drag and lift-to-drag ratio, both the major parameters in wing design. The numerical and experimental results show that the novel design of the lattice wings has distinct advantages in comparison to the conventional not-swept configurations. Compared to conventional lattice wings the maximum benefit e.g. of the zero-lift total drag for the investigated locally swept lattice wings is of the order of 30% - 40%.

1.0 INTRODUCTION

Grid fins (also called lattice wings or lattice controls) are compact constructions of several aerodynamic surfaces (members), which are held together by a common framework and build a versatile aerodynamic device. This device can be used as aerodynamic stabiliser, lifting or control element (Figure 1a). Each member usually represents a very thin high-aspect-ratio rectangular wing of constant chord. Additionally to the shape of the used basic airfoils, the grid fins can generally be described by a number of geometrical parameters such as span, height, chord, member thickness and cell spacing.

Lattice wings are admittedly unconventional, but not really unknown aerodynamic devices. The construction of the lattice wings is derived from the kites that were known in China already in the first century B. C.. Just about hundred years ago the aeronautics pioneers A. Santos Dumont (1906) and Horatio Phillips (1908) used lattice wings as lifting surfaces and stabilisers for their first motorised flight attempts. At present the applications of lattice wings ([1], [2]) include hydrofoils at low speeds and, above all, ballistic missiles and projectiles, as well as singular highly agile guided missiles at high speeds (Figure 1b).

Schülein, E.; Guyot, D. (2006) Novel High-Performance Grid Fins for Missile Control at High Speeds: Preliminary Numerical and Experimental Investigations. In *Innovative Missile Systems* (pp. 35-1 – 35-28). Meeting Proceedings RTO-MP-AVT-135, Paper 35. Neuilly-sur-Seine, France: RTO. Available from: http://www.rto.nato.int/abstracts.asp.

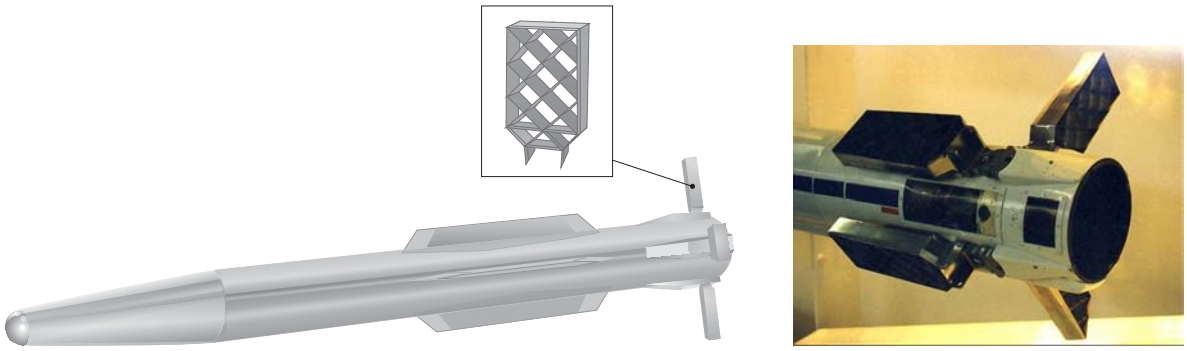

a. b. Source: [7]

Figure 1: Sketch of a missile with grid fins as tail control device (a) and a photo of folding grid fins on R-77(AA-12) missile (b).

In the last 20 years, after the publication of the fundamental Russian book about the grid fins [1], this topic has been the object of intensive investigations in the scientific community working on missile technology in some NATO countries. Several studies on lattice wings have been carried out in USA, UK, Canada, France and Germany. Some papers presented at the RTO AVT Panel Symposium in Sorento (Italy, 1998) were focused on this topic [3]-[6].

Since the middle 90's, several research activities have been conducted also at the German Aerospace Center DLR. Like most research programs on lattice wing technology at that time, the target of the extensive studies at DLR was not only the removal of the lack of knowledge, but also the development of reliable tools for design and optimisation of lattice wings. The wind tunnel experiments (e.g. [8], [9]) enabled the establishment of a large database for different basic configurations of lattice wings over a broad range of flow conditions: Mach numbers from 0.3 up to 6.0, angles of attack from 0 to 90 degrees and angles of yaw from 0 to 30 degrees with the target to check the statements propagated in [1] and to collect further know-how about this technology. On the basis of the experimental data the half-empirical lattice wing theory was fitted and validated [10]. With the subsequent developed software module "FastGRIDS" and its implementation as an actuator disk into the unstructured Navier-Stokes-solver TAU [11] a new fast numerical tool for aerodynamic design and optimisation of missile configurations with lattice wings was developed [12]. This tool was validated with experimental data obtained in the wind tunnel on missile models with grid fins ([13], [14]) and saves over 80% time for the complete calculation of realistic missiles [15].

The reasons for the interest in lattice wing devices are its unique aerodynamic and structural characteristics, which offer, in comparison to the conventional monoplane surfaces, a combination of some benefits and drawbacks. The advantages are in particular (see e.g. [1]-[7], [16]): 1) the high aerodynamic effectiveness at low weight and volume; 2) well adjustable aerodynamic characteristics for wide ranges of Mach numbers and deflection angles; 3) enhanced yaw stability at high incidence angles and improved roll stability; 4) small hinge moments with minimal shift of the centre of pressure; 5) compact size and possibility to be folded down to the fuselage (Figure 1b) making the missile more compact and easier to store or transport. The biggest disadvantages of these wings are their relatively high drag levels at given lift characteristics as well as the weak stability at transonic speeds. The first one emerges because of the multi-plane construction of grid fins. The second disadvantage is due to the chocking of the cell flow in the transonic regime, which happens because of the typical rectangular form of each grid fin cell. These are serious disadvantages and can have a negative effect on realistic applications. If, for example, favourable aerodynamic effectiveness and yaw stability at high incidence angles are making lattice wings very attractive for high-speed agile missiles, the substandard wave drag is completely discrediting it in this situation. Therefore, the high speed applications of lattice wings are

actually undisputed only as drag braking devices or stabilisers for control of bombs and dispensers or as control elements for very-short-range missiles where the high resistance certainly plays only a minor role. So, in the last years grid fins were implemented e.g. on the biggest non-nuclear Massive Ordnance Air Blast (MOAB) bomb as well as on smaller high-precision Joint Direct Attack Munitions (JDAM) or "smart" bombs, where they stabilise and steer the weapon to a target using GPS signals for guidance.

The usual wave drag reduction approaches for conventional lattice wings are the minimisation of leading edge bluntness and total surface thickness [17], both typical for common nose wave drag reduction measures [18]. For lattice control elements at supersonic missiles, either wedge, double-wedge or hexagonal profile airfoils with extremely sharpened leading edges and thinned surfaces are usual chosen correspondingly (see e.g. [1]). The request for very thin surface elements with leading edges as sharp as possible lead to very high manufacturing costs for drag optimised lattice wings and, consequently, cannot be accepted in most real applications. The aerodynamically optimal profile of the airfoil, which reaches drag levels below the simple sharp case due to local flow overexpansion [18], is of exactly defined and very small nose bluntness. The industrial manufacturing of such precise nose contours at thin surfaces is even less realistic. Furthermore, the enormous thermal and mechanical loads on the sharp leading edges associated with higher supersonic speeds restrict the possibilities to use such strips of thin metal sheets as construction elements of grid fins. The melting or burning loss on the leading edge material at these speeds will damage the optimised contour within a very short time only. Consequently, the reduction of the lattice wing's drag is still very important and means a clear improvement of the lattice wing performance.

2.0 WAVE DRAG REDUCTION APPROACH

One of the characteristics of conventional grid fins is the *unswept* rectangular-shaped plan form of its basic internal members. The advantages of swept leading edges for the planar wings or control surfaces in contrast to unswept ones are already known for about sixty years [19]. Its aerodynamic wave drag due to thickness at higher supersonic speeds is only a small part of a comparable rectangular wing. So, the zero-lift wave drag of a rectangular wing at a Mach number $M_\infty = 1.5$ is already approximately 2.5-time higher as of a comparable delta wing with $\varphi = 70°$ [20], where φ is the leading edge sweep angle. The corresponding maximum lift-to-drag ratio of a rectangular wing is only about 61% from the mentioned delta wing. For higher Mach numbers the profit is even higher. Another important advantage of the planar swept wing is a clear improvement of the transonic speed behaviour.

The effect of the leading edge sweeping can simply be explained as follows. It is well known, that in the case of the rectangular wing with given airfoil profile (Figure 2a) the intensities of the appearing compression shocks and expansion waves and, consequently, the surface pressure distribution and wave drag are determined only by the free-stream Mach number M_∞. For the swept wing (Figure 2b) the free-stream Mach number M_∞ can be divided into two components, one parallel to the leading edge $M_{//}$ ($M_{//} = M_\infty \sin\varphi$) and the other one normal to it $M_\perp$ ($M_\perp = M_\infty \cos\varphi$). Apart from the local effects at the wing's leading edge, which are not considered here, the flow parallel to the leading edge has no effect on the wall pressure distribution. The normal component, the so called effective Mach number $M_\perp = M_{eff}$, destines the surface pressure distribution. From $M_{eff} < M_\infty$ follows a weaker bow shock intensity and therefore a lower wave drag for swept wings. The bigger the sweep angle or the free-stream Mach number M_∞, the bigger this effect is. However, for incident swept wings not only the pressure drag but also the lift is reduced, the change of the drag is dominating and the lift-to-drag ratio for the swept wing is essentially higher than for a comparable rectangular wing [20]. That is the second advantage of a swept wing.

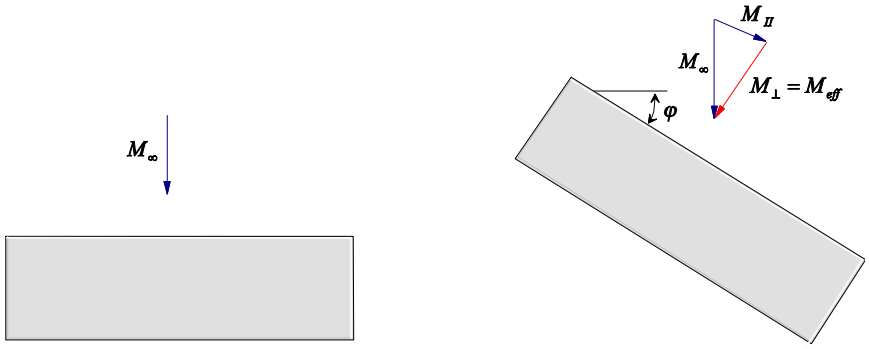

a. b.

Figure 2: Flow conditions around of rectangular unswept (a) and swept (b) wings.

The investigations of the globally "swept" or "yawed" grid fins are also known (see e.g. [1],[8],[9],[21]). In opposite to conventional planar wings, the swept grid fin shows a clear increase in wave drag. This, on the first glimpse unexpected, trend can clearly be explained with the observation of the flow over individual grid members. Through the grid structure, this swept orientation of the outer framework, which is really a deflected grid fin, actually leads to the increase of the local incidence angles for some internal members and, consequently, to a distinct increase in the total wave drag of the grid fin.

According to ideas presented in [22] the effective leading edge sweep for a grid fin can only be reached if the leading edges of each internal member are locally swept. The plan-form of all members has to be similar to a row of delta wings located side-by-side (Figure 3). Corresponding lattice wing configurations, which are assembled from internal members with locally swept edges (LSEs), should have the advantages of swept wings in the grid fin technology. Figure 4 presents the two most simple grid fin configurations with locally swept leading edges that differ only in the position of the tooth relatively to the grid cell. According to [22] different other configurations are possible by varying the main geometrical parameters: the relative size of each periodical "tooth", its number and position within the grid cell, as well as the locally sweep angle. To the authors knowledge there are no investigations on similar locally swept grid fins up to now. This kind of lattice wings is expected to be more favourable for the use at high speeds as the conventional configurations.

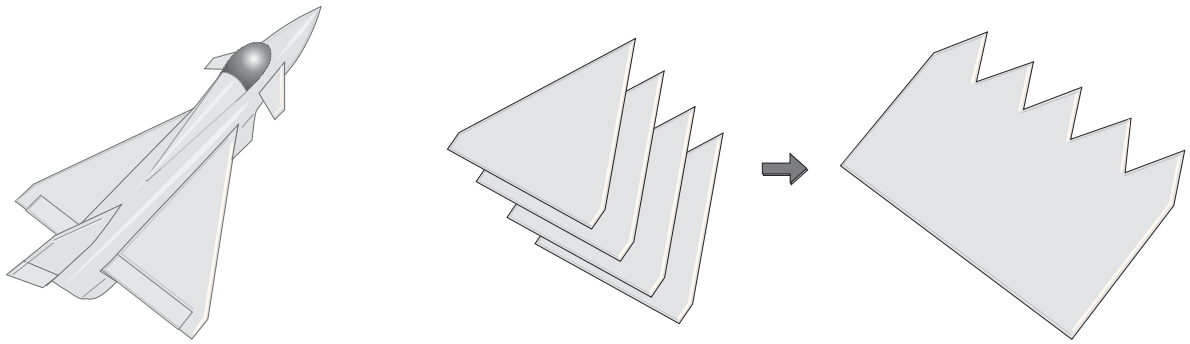

a. b.

**Figure 3: Typical configuration of a jet fighter with delta wing
(a) and generation of the LSE geometry as a row of delta wings (b).**

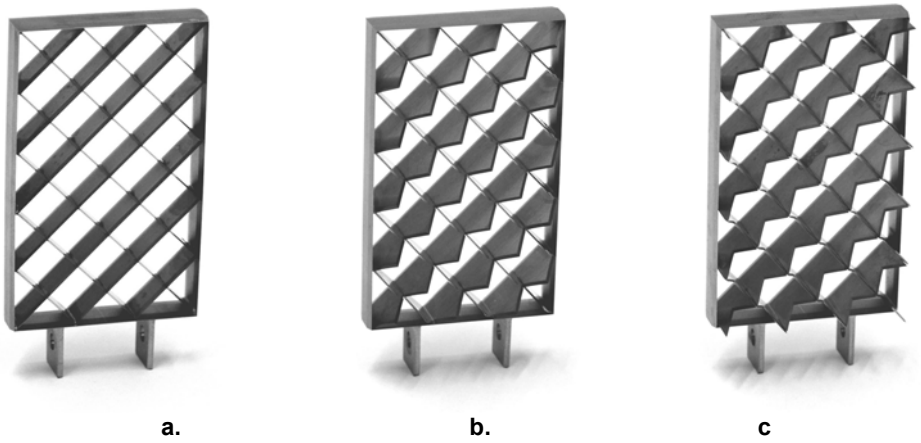

a. b. c

Figure 4: Typical unswept (a) and two locally swept grid fins (b, c).

The object of the present work is a parametric study of locally swept wing configurations regarding its performance at high speeds. The preliminary investigations include numerical simulations of a supersonic flow around the conventional and locally swept planar and lattice wings of infinite span, which were performed within the framework of a diploma thesis [23], as well as wind tunnel experiments on corresponding realistic finite span models. The examination on the planar wings additionally to the lattice controls should show the potential and the influence of each geometrical parameter that characterises the LSE form – sweep angle as well as the relative tooth size in span and chord direction. Investigations include also some additional parameters, e.g. the relative tooth position within the grid cell, whose effect could be analysed only for complete grid fin configurations (see Chapter 3.2).

3.0 INVESTIGATED LOCALLY SWEPT WING MODELS

A big number of planar and lattice wing geometries were investigated in the present work. The model geometries and configurations were not always the same for numerical and experimental simulations. Therefore, brief definitions for the creation of the model names that will occur in the description of the results are given here.

3.1 Definition of the geometrical parameters for the locally swept wings (LSWs)

Figure 5 sketches the geometry of a locally swept planar wing with a hexagonal cross section profile. The typical parameters for the description of a conventional rectangular wing are: chord c, span s, thickness t, half-angle of the leading (LE) and trailing (TE) edge sharpness, measured in the plane normal to the edges β_{nLE} and β_{nTE}.

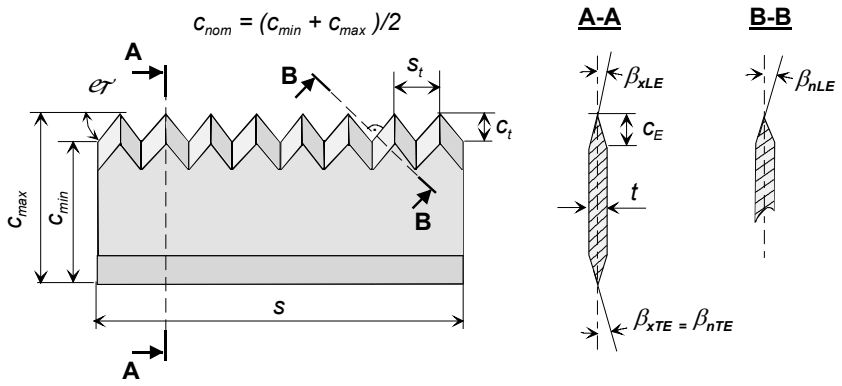

Figure 5: Geometry of locally swept planar surfaces.

For the locally swept configurations some additional parameters are necessary: sweep angle φ, tooth length c_t and nominal wing chord c_{nom}. In the presented case the tooth length can be determined by $c_t = c_{max} - c_{min}$. The nominal wing chord marks the chord of a comparable rectangular wing with the same lifting surface and can be determined for given configuration as $c_{nom} = (c_{min} + c_{max})/2$. These parameters specify the geometry of the LSE planar wing completely. The secondary geometrical parameters like relative tooth length ξ and tooth size σ, the half-angles of edge sharpness β_{xLE} and β_{xTE}, as well as the length of the corresponding edge c_E and tooth width s_t, describe the LSE wing geometry additionally. The angles β_x, measured in the plane x-z, describe the sharpness of the edges in free-stream direction. They can be derived from the corresponding angles β_n at given sweep angle as $\beta_n = \tan^{-1}(\cos\varphi \tan\beta_n)$.

The relative tooth length ξ and the relative tooth size σ mark the relations of the tooth length to the wing's chord ($\xi = c_t / c_{nom}$) and to the wing's edge length ($\sigma = c_t / c_E$). Both relations express different aspects of the LSE shaping. The first parameter ξ characterises the global plan-form of a LSW. From the view of the usefulness for realistic applications, the small ξ values should be very desirable since that means small chord length variations at given lifting surface for small hinge moments with minimal shifts of the centre of pressure. The second parameter σ is an expression of the tooth size relative to the wing thickness. Very small values of σ make little sense, because such locally swept wing will transform to a rectangular wing with a fine grooved nose. Therefore it is very important to reach relatively moderate σ values at small ξ values. Consequently, the optimal locally swept edge configuration can be found from the compromise of these two parameters, because for given wing thicknesses t and angles β_n and φ the relative tooth size σ is a linear function of the relative tooth length ξ, so that $\sigma = (2c_t \cos\varphi \tan\beta_n)/t = (2\xi c_{nom} \cos\varphi \tan\beta_n)/t$.

3.2 Definition of the geometrical parameters for the locally swept lattice wings (LSLW)

As described above the conventional grid fins can generally be defined by a number of geometrical parameters such as span s, height h, chord c, member thickness t and cell spacing. For locally swept lattice wings additional parameters as presented in the previous chapter are needed for the description of the member's geometry.

The arrangement of the members to the lattice structure requires at least two new parameters: the relative tooth position for crossing members and the number of teeth n_t inside of each grid cell. The most simple configurations of locally swept grid fins, presented in Figure 4, have a single tooth per cell ($n_t = 1$) and two different arrangements of teeth at the intersection of crossing members. The first one in Figure 4b presents a configuration of *peak-type* and the second – of *valley-type* (Figure 4c). The applied logic for this definition is explained in Figure 6, where two regular types of intersection for crossing locally swept

planes are presented in detail. The flow direction is meant to come from top to bottom. For the peak-type both crossing teeth have a common peak between four valleys (Figure 6a), and for the valley-type corresponding – a common valley between four peaks (Figure 6b). These two types of member intersection should be sufficient for all symmetrical cases with integer numbers of teeth in each grid cell. There are some other combined variations of these types imaginable, which have not been considered in this paper.

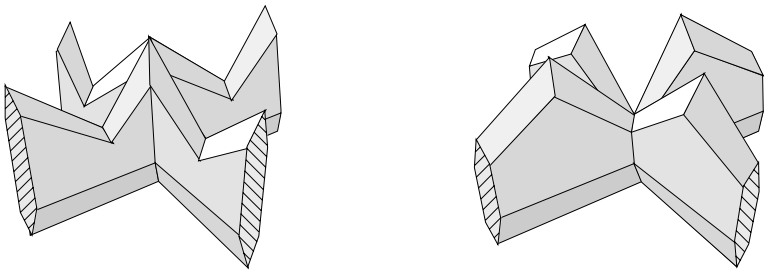

a. "Peak"-type **b. "Valley"-type**

Figure 6: Definition of the member intersection-types for locally swept grid fins.

3.3 Definitions of investigated models

The common name for the investigated locally swept planar wings includes some main parameters, which enables a sufficient description of the leading edge geometry in the shortest form: LSW$\beta_n_\varphi_\xi$. For example, the name LSW$_{10°_55°_0.357}$ defines a wing with $\beta_n = 10°$, $\varphi = 55°$ and $\xi = 0.357$. As for an unswept rectangular wing the introduced parameters are $\varphi = 0°$, $\xi = 0$, $\beta_n = \beta_x$, this wing at $\beta_n = 10°$ should be declared unequivocally as LSW$_{10°_0°_0}$ or simply RW$_{10°}$ (with RW for rectangular wing). All numerically and experimentally investigated planar wings have a common half-angle of normal leading edge sharpness $\beta_n = 10°$. Some other major parameters including wing thickness t, chord c and span s were varied. The influence of the local sweep parameters like φ, ξ and σ was investigated by its independent variation.

The selection of the investigated lattice wing configurations was limited due to high costs of precise manufacturing of wind tunnel models. Without being exhaustive, the common name for the investigated locally swept lattice wings are created similarly to planar wings as LSLW*type*_$\beta_n_\varphi_\xi$. The *type* means the type of plane intersection: *"p"* for *peak*- and *"v"* for *valley*-type. Because of the relatively big number of main parameters for lattice wings, not all parameters could be included in the name of the investigated wings. These parameters will be declared separately in the text. An important simplification of the numerical models was the neglect of the outer framework influence, so that only grid fins of infinite height h and span s could be investigated numerically. The experimental models are manufactured comparable to conventional grid fins and have an outer framework with locally swept edges. Some examples of the used lattice wing wind tunnel models are shown in Figure 4.

4.0 NUMERICAL SIMULATION TOOLS

The numerical simulations have been performed with the TAU-code [24], an internal development of the German Aerospace Centre (DLR). The TAU-code solves three-dimensional Navier-Stokes equations using a finite volume approach and can handle structured, unstructured and hybrid meshes. The time integration is carried out through the explicit Runge-Kutta scheme. The model geometries were transposed by means of the CAD-program ARGON® and the grids required for the calculation have been generated with the commercial grid generation package CENTAUR® that provides hybrid meshes with structured and unstructured parts. In the present work only unstructured meshes were used. The solid wall surfaces were discretised by triangles and the 3-D flow field correspondingly by tetrahedrons. For fast and effective

numerical calculations of numerous investigated wing configurations and flow conditions, some simplifying assumptions were made. Firstly, the solid surfaces of the wings were created as "inviscid Euler wall" boundary condition. Secondly, the calculations were made for infinite wings without effects of the lattice wing framework or wing tips. And thirdly, the leading edges of the models were assumed to be absolutely sharp. These conditions are sufficient to prove the effect of the local leading edge sweep on the wave drag reduction without the relinquishment of the important flow phenomena.

5.0 WIND TUNNEL

The experimental part of the work was carried out at the Ludwieg-Tube Facility in Göttingen (RWG) [25]. This supersonic/hypersonic wind tunnel covers a Mach number range of $3 \le M \le 7$ and a unit Reynolds number range between $5 \cdot 10^6$ m^{-1} and $80 \cdot 10^6$ m^{-1}. The technique was originally developed by Hubert Ludwieg more than fifty years ago [25]. The facility consists of an 80-meter long tube used as pressure reservoir which is separated from the nozzle and the test section by a quick-acting gate valve. Downstream the valve a supersonic nozzle leads to the test section followed by a dump tank. After opening the gate valve an unsteady expansion wave propagates with the speed of sound through the pressurised test gas. Behind this wave the gas exits the tube at constant stagnation conditions. The expansion wave is reflected at the closed end of the tube and finally reaches the nozzle throat again so the run time of the facility is given by the actual speed of sound and twice the tube length. A main advantage of this technique is the absence of disturbance-producing devices such as pressure regulating valves or grids located upstream of the nozzle. The technical data of both tubes can be taken from Figure 7. Supersonic flow is generated by individual nozzle blocks. The test section for the Mach numbers M = 3 and 4 has a cross section of 0.5×0.5 m^2 and at M = 5 and 6 a circular test section with a diameter of 0.5 m.

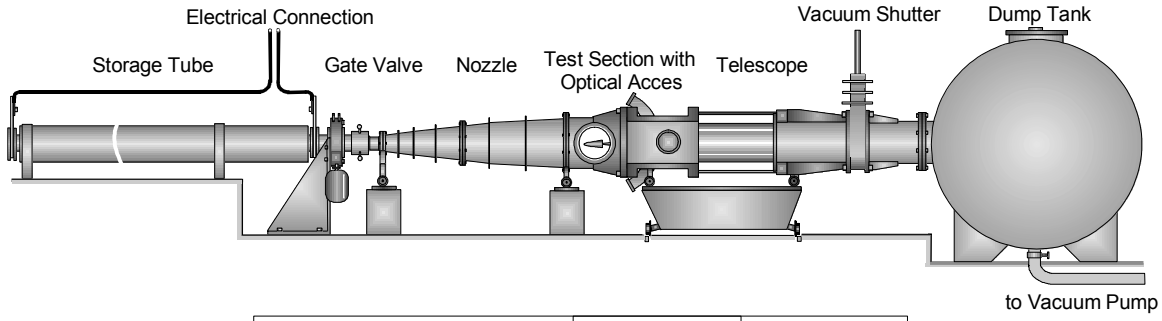

Performance	Tube A	Tube B
Max. Stag. Pressure, bar	15	40
Max. Stag. Temperature, °C	20	400
Mach Number	2.79 to 4.65	5.0 to 6.9
Unit Reynolds Number, 10^6 m^{-1}	5 to 60	5 to 50
Run Time, s	0.4	0.3
Test Section	0.5 x 0.5 m²	⌀ 0.5 m

Figure 7: The RWG Ludwieg Tube Facility in Göttingen.

6.0 RESULTS FOR LOCALLY SWEPT PLANAR WINGS

6.1 Numerical investigations of LSW

The influence of the local sweep angles φ and of the relative tooth length ξ on the LSW performances was investigated numerically for a Mach number range from 2 to 6 and an Angle of Attack (AoA) from 0° to 10°. The names of the studied wings include the main geometrical parameters of the locally swept edges described in chapter 3.1. The other common geometrical parameters, such as wing thickness t = 0.5mm,

span $s = \infty$, the half-angle of normal edge sharpness $\beta_{nLE} = \beta_{nTE} = 10°$ and nominal chord length c_{nom} = 10mm were held constant for all investigated test-cases.

Wing's wave drag and lift are determined by the surface pressure distribution. At $\alpha = 0°$ the pressure drag of the wing can be obtained directly from the pressure difference between their nose and rear parts. Figure 8a shows the distribution of the pressure coefficient for a rectangular unswept wing $RW_{10°}$, which is independent from y and characterises approximately a two-dimensional flow. The increased surface pressure levels on the nose part (red area) changes downstream to approximately free-stream pressure levels on the flat part of the wing (green area) and finally to the low pressure levels on the rear part (blue area). Figure 8b and 8c show significantly lower pressure levels on the nose parts of the locally swept wings with $\varphi = 55°$ and 70° for the investigated constant nominal chord length of c_{nom}= 10mm and nose half-angles of $\beta_n = 10°$. As expected, the increase of the swept angle φ leads to a decrease of the nose pressure levels. The rear part pressure levels remains approximately constant for the shown tooth-wings. It follows that the investigated LSW's with higher swept angles φ create a lower pressure drag.

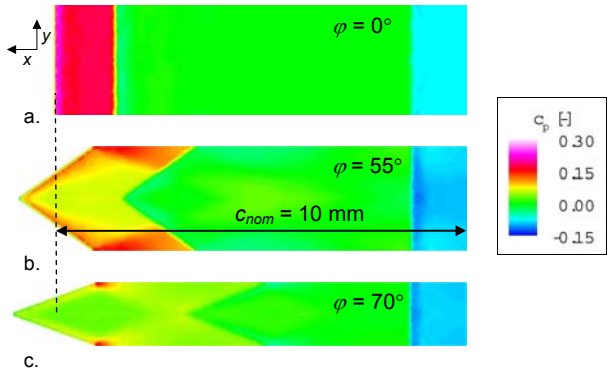

Figure 8: Effect of the local sweep angle φ on the pressure coefficient distribution at Mach number $M_\infty = 3$ and $\alpha = 0°$: a) $\varphi = 0°$, $RW_{10°}$; b) $\varphi = 55°$, $LSW_{10°\_55°\_0.179}$; c) $\varphi = 70°$, $LSW_{10°\_70°\_0.179}$.

The influence of the relative tooth length ξ at constant test conditions is demonstrated in Figure 9. The common nominal chord length c_{nom} is shown on the picture for all wing configurations. It is remarkable that in principle the pressure distribution at the nose part shows three areas with different pressure levels, corresponding to yellow-green, orange and red colours (Figure 9).

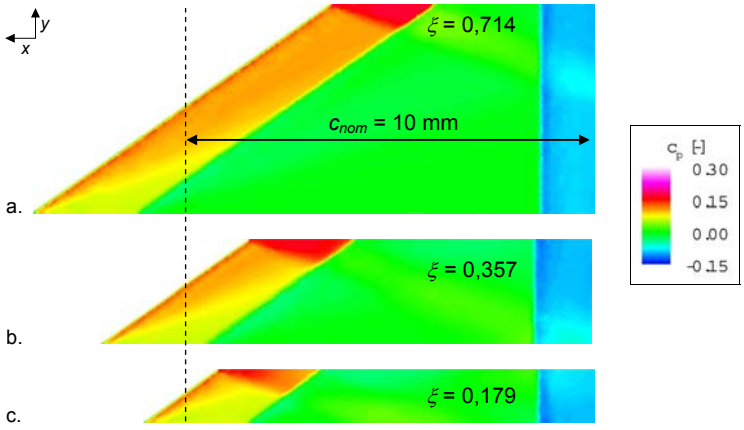

Figure 9: Effect of the relative tooth length ξ on pressure coefficient distribution at Mach number $M_\infty = 3$ and $\alpha = 0°$: a) $\xi = 0.714$, $LSW_{10°\_55°\_0.714}$; b) $\xi = 0.357$, $LSW_{10°\_55°\_0.357}$; c) $\xi = 0.179$, $LSW_{10°\_55°\_0.179}$.

The decrease of the tooth length led to a decay of the middle-pressure area. The sizes of the other two areas remain constant. To explain the origin of these differences in pressure levels the sketch of the flow structure near a locally swept leading edge is demonstrated in Figure 10. The flow regions of the locally swept leading edge indicate areas of 2-D swept flow (A), of reduced wave intensities (B) and of amplified wave intensities (C). So, region A includes the uniform 2-D flow behind the attached flat bow shock, similar to the flow on a swept wing of infinite aspect ratio. For region B the conical flow theory can be applied for the approximate calculation of the inviscid flow parameters. This region lies within the upstream Mach cone originating from the wing's tip. The Mach angle $\mu = arcsin(1/M_2)$ characterises the limit for the spreading of pressure disturbances generated at this point, where M_2 stand for the local Mach number behind the bow shock wave. The region of the highest nose pressure C is located behind the crossing shock waves, which are coming from the neighbouring tooth. The angle of the local shock wave inclination ω can be determined relative to the flow direction in region A. Although the real surface pressure distribution is of cause more complicated and influenced by wave / boundary layer interactions, this very simplified flow model shows the main physical effects. The relative sizes of all three regions assign the resulting average nose pressure level or, correspondingly, the wave drag due to thickness for planar tooth-wings. As will be shown below the smaller teeth are more effective for wave drag reduction approaches.

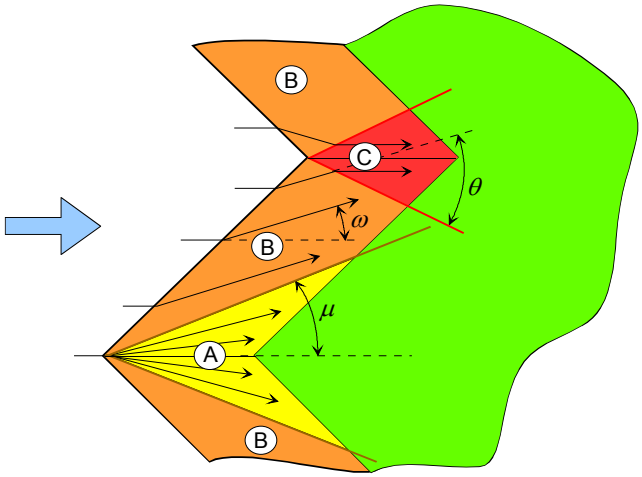

Figure 10: Different flow regions on the locally swept leading edge: A- 2D swept flow; B- region of reduced wave intensities; C- region of amplified wave intensities (μ - Mach angle; θ - local shock wave inclination angle, ω - local flow deflection angle).

For a better demonstration of the spatial extension of shock and expansion waves and their mutual interaction areas, the calculated Mach number distributions in different cross-sections on the wing $LSW_{10°\_55°\_0.357}$ are shown in Figure 11 at free-stream Mach number $M_\infty = 3$ with and without angle of attack. The different cross-sections from A to F characterise the development of the flow with increasing coordinate x. The x -coordinate for each cut is declared in corresponding plots and shown schematically in the plan view of the wing. For the case without AoA the Mach number distribution on the upper and lower side of the wing is identical, therefore only the area above the wing is presented. The cut through the wing itself is represented in all illustrations as black area.

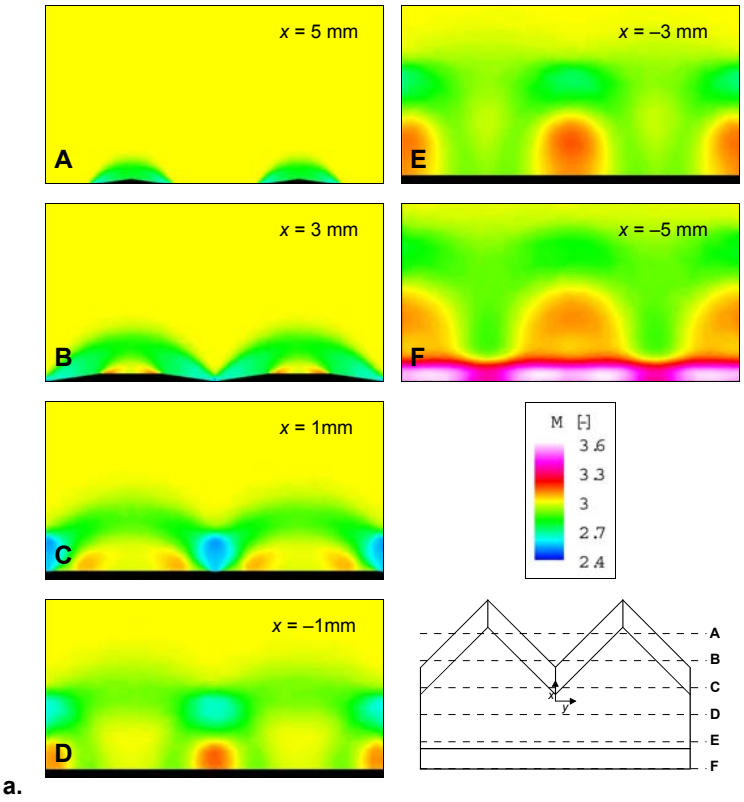

a.

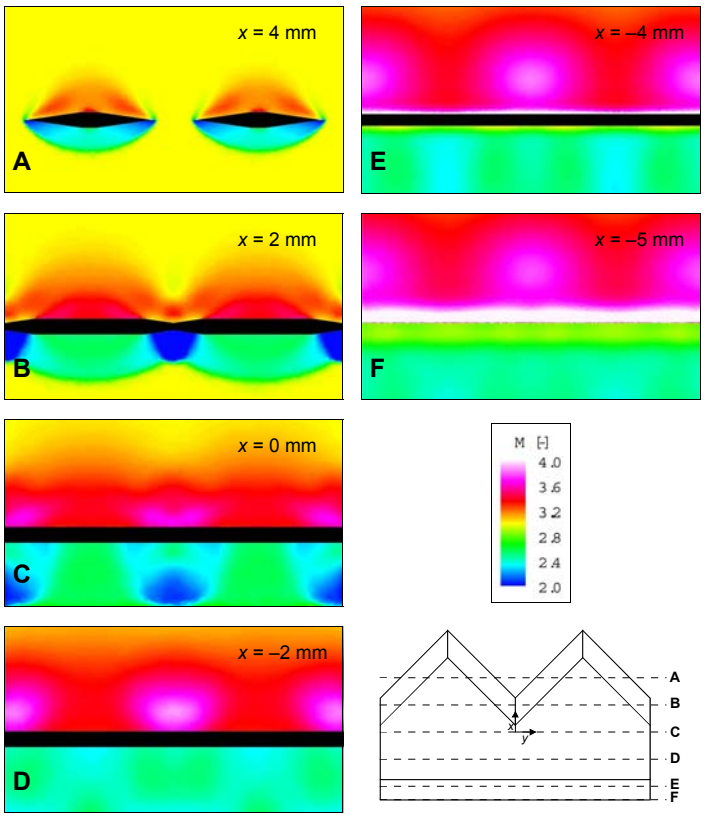

b.

Figure 11: Mach number distributions in different cross-sections A-F on the wing $LSW_{10°\_55°\_0.357}$ at Mach number $M_\infty = 3$ and $\alpha = 0°$ (a) and $\alpha = 10°$ (b).

In contrast to the nominal 2-D flow near an unswept rectangular wing the investigated flow around the LSW has clearly a 3-D character. The three-dimensionality of the wave fronts can be identified in all chosen cross sections. The numerical calculations show that shock wave intensities generated by the locally swept leading edges are weaker as on the reference rectangular wing $RW_{10°}$ (results not shown here). The bow shock intensities can be derived from the Mach number levels behind the shock. The reason for the weaker bow shock intensities is the expected smaller effective Mach number on the basis of the swept leading edge as well as the additional attenuation of the waves due to its conical form near the tooth peaks as described above. The high pressure regions behind crossing shock waves discussed in Figure 10 (region C) are visible in Figure 11 through lower Mach numbers in flow fields between neighbouring teeth.

To quantify the improvement of the performance for locally swept planar wings in comparison to the well known rectangular ones, the aerodynamic force coefficients are compared with the ones for the reference rectangular wing, so that e.g. a relative profit in the wave drag could be quantified like:

$$\text{Relative wave drag reduction} = \frac{c_{WD}\left(\text{LSW}_{10°\_\varphi\_\xi}\right) - c_{WD}\left(\text{RW}_{10°}\right)}{c_{WD}\left(\text{RW}_{10°}\right)} 100\% .$$

The profits in the lift and in the lift-to-drag ratio can be determined similarly and therefore the corresponding equations are not presented here.

Figure 12 and Figure 13 show the wave drag coefficients and the relative wave drag reduction obtained from the described numerical simulations for the locally swept planar wings as function of the Mach number without angle of attack. These plots present the effects of sweep angles (Figure 12) and of the relative tooth length (Figure 13) on zero-lift planar wing performances.

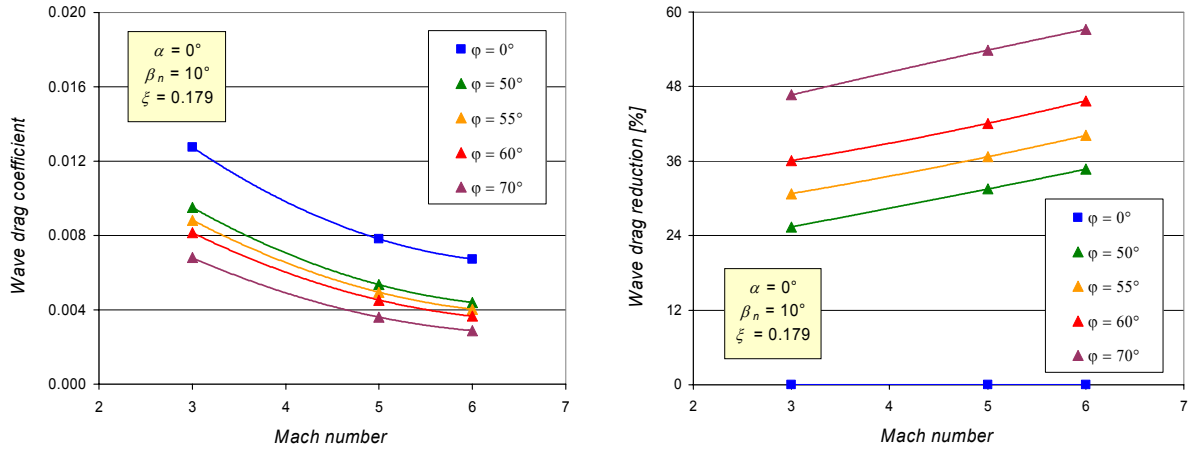

Figure 12: Influence of the sweep angle φ on the wave drag coefficient (left) and on the relative wave drag reduction (right) vs. Mach number at α = 0°, ξ = 0.179, β_n = 10°.

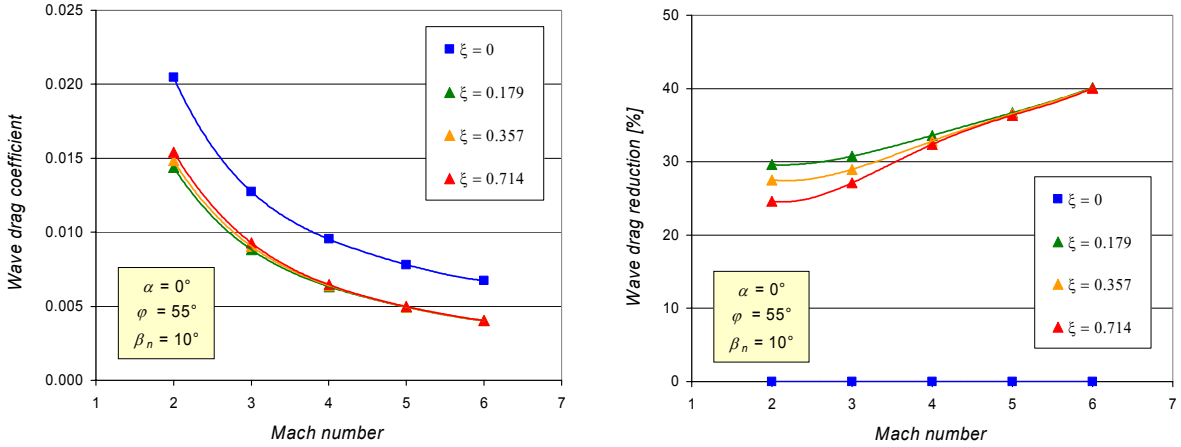

Figure 13: Influence of the relative tooth length ξ on wave drag coefficient (left) and on the relative wave drag reduction (right) vs. Mach number at $\alpha = 0°$, $\varphi = 55°$, $\beta_n = 10°$.

At incidence the lift-to-drag ratio is a more meaningful parameter for wings with $\alpha > 0°$ since it takes not only the drag but also the corresponding lift alteration into account. Figure 14 shows the Mach number dependence of the lift-to-wave-drag ratio and its additional improvement relatively to the reference wing. As the skin friction drag is not considered in this calculation, the presented parameter only gives a qualitative statement of the performance of locally swept wings.

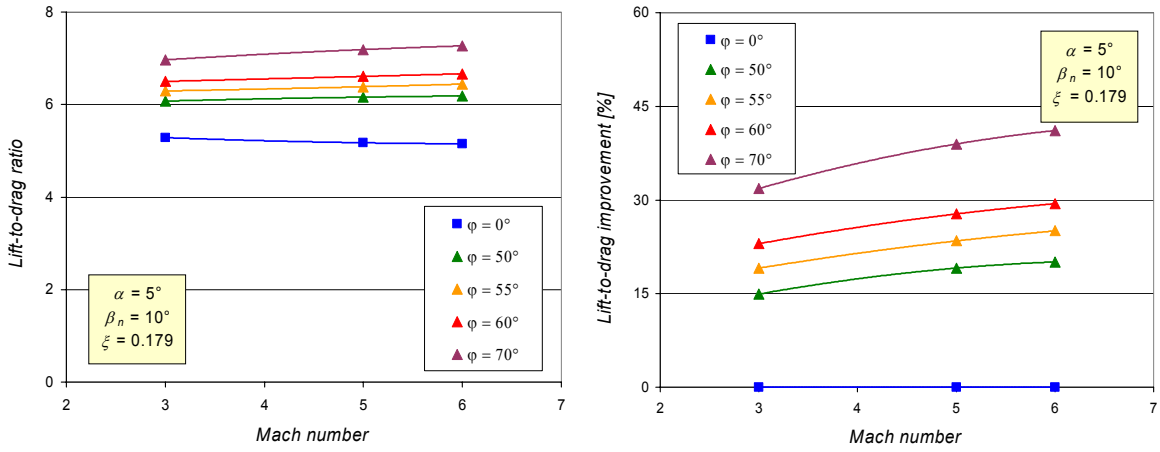

Figure 14: Influence of the sweep angle φ on lift-to-drag ratio (left) and on the relative lift-to-drag improvement (right) vs. Mach number at $\alpha = 5°$, $\xi = 0.179$, $\beta_n = 10°$.

The observed behaviour of the wave drag and of the lift-to-wave-drag ratio completely confirms the expected effect of the locally swept leading edges. The reduction of the zero-lift wave drag as well as the improvement of the wing's lifting performances increases with the Mach number and with the local sweep angle and weakly decreases with the relative tooth size. The common quantitative presentation of these tendencies for Mach numbers 3 and 5 on the results of the numerical calculations is given in Figure 15.

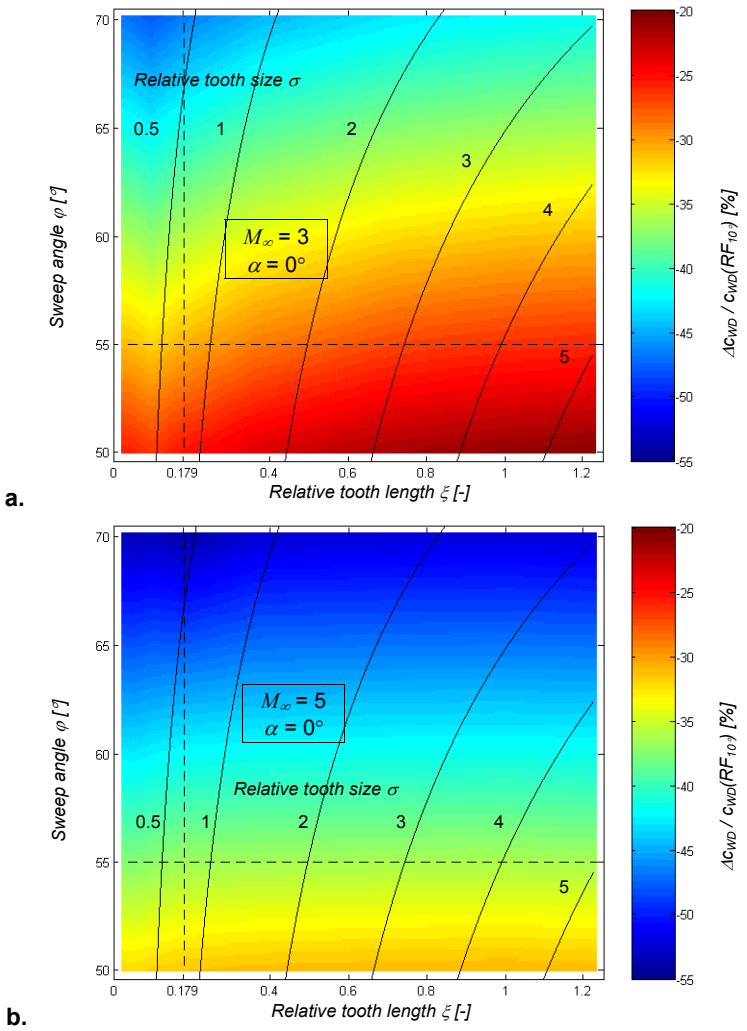

Figure 15: Benefit of the wave drag vs. sweep angles and relative tooth length at α = 0° for Mach numbers M_∞ = 3 (a) and M_∞ = 5 (b) at β_{nLE} = 10°.

The presented contour plots are produced with the help of interpolated distributions of wave drag reduction values in sweep angle φ- and relative tooth length ξ- coordinates. The positions of the LSW geometries with defined values of relative tooth sizes σ for the investigated wing thickness are shown on these plots by solid lines. As described earlier in chapter 3.1 for given wing thicknesses t and nose sharpness half-angles β_{nLE} the relative tooth size σ is a linear function of the relative tooth length ξ and cosine of the sweep angle $cos\varphi$. This presentation offers a good possibility to pick out the most favourable configuration for given conditions for the remaining free local sweep parameters. As an example, a combination of sweep angles of 55° and of a relative tooth length of 0.179 (crossing dashed lines) was selected for the numerical investigations of locally swept lattice wings described below.

The clear profits of up to 57% in the wave drag as well as up to 41% in the lift-to-wave-drag ratio confirm the assumed high potential of the local leading edge sweeping. The effects found of the flow parameters (Mach number and angle of attack) and of the geometrical wing parameters (sweep angle and relative tooth length) on the wing performances can be explained on the basis of the numerically obtained distributions of surface and flow field parameters. To find out whether the numerical results also apply to real wings and have not been falsified by the simplifications direct force measurements were obtained in wind tunnel tests. The results of these measurements are discussed in the next chapter.

6.2 Results of experimental investigations of locally swept planar wings

The experimental investigation of the LSW performances was obtained in the Ludwieg Tube Facility RWG at two Mach numbers $M_\infty = 3$ and 5 for three angles of attack 0°, 5° and 10°. All in all 25 different wing configurations were investigated during the tests. Some geometrical parameters of the investigated wings, like local sweep angle φ, the relative tooth length ξ and wing thickness t, have been varied. The other common geometrical parameters remained constant or were varied for technical reasons. So the half-angle of normal edge sharpness $\beta_{nLE} = \beta_{nTE} = 10°$ and nominal chord length $c_{nom} = 50$mm were held constant for all investigated test-cases. The span of the wings s was initially chosen as a corresponding full-tooth number distance, which is as closely as possible to 100mm or 150mm. For subsequent reference tests, which were needed for the elimination of the sting- and tip-influences, the span of all wing models were shortened after the first test campaign in the work shop so that some outer teeth were removed before the final tests were started. Figure 16 shows a typical example of a locally swept planar wing model before and after the cutting off. Most locally swept wing configurations were manufactured with two different thicknesses t of 2.5mm and 3.5mm for the additional examination of the relative wing thicknesses effect.

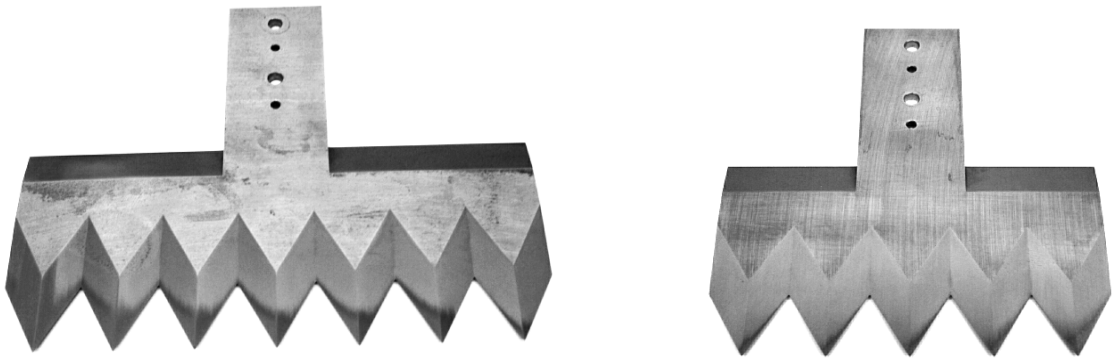

a. b.

Figure 16: Two typical locally swept planar wing models for RWG wind tunnel tests with different span width for the adjustment of the force measurement results.

The typical results of force measurements on locally swept wings are presented in Figure 17. Influence of sweep angles on the total zero-lift drag coefficients and on the relative reduction of the total drag confirm the tendencies observed in the numerical results. For the investigated moderate tooth length of $\xi = 0.357$ the measured total drag shows relatively high benefits versus sweep angles between 0° and 70°. As expected, the increase of the relative wing thickness led to higher total drag reduction levels. The improvement demonstrated on the planar wing performances at realistic flow conditions has the same order as the calculated results based on calculations with inviscid wall conditions. So if the experimental results in Figure 17 for LSW ($\xi = 0.357$, $\beta_{nLE} = \beta_{nTE} = 10°$, $t/c_{nom} = 0.05$) at Mach number 5 without angle of attack show a reduction of the *total* drag in the order of 28%-38%, then a comparable LSW at the same flow conditions (Figure 15b) shows a *wave* drag reduction of about 32%-50% in the numerical simulations. For smaller tooth length and bigger sweep angles the improvement of the wing performance is even more significant.

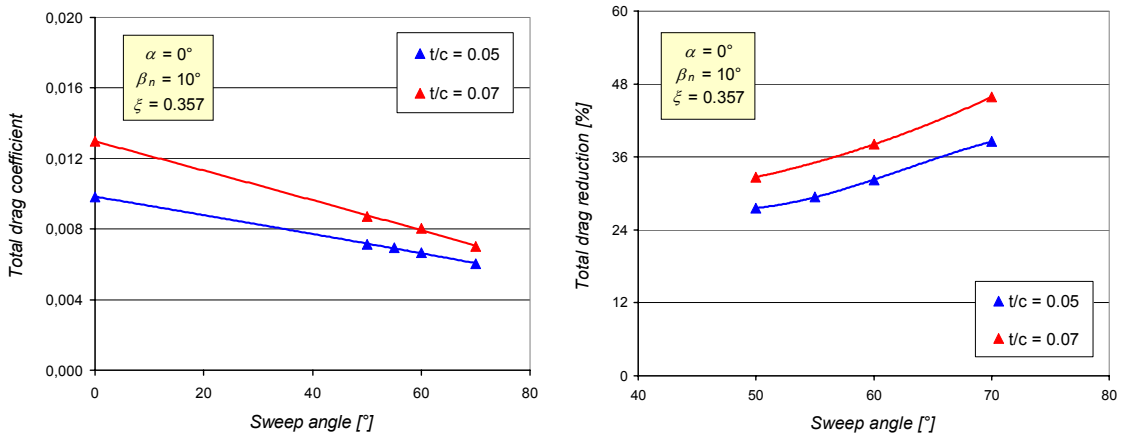

Figure 17: Measured total drag of locally swept planar wings vs. sweep angle at $\alpha = 0°$ for two relative thicknesses t/c_{nom} at Mach number $M_\infty = 5$ and $\beta_{nLE} = 10°$.

Furthermore, the experimental results confirm the influence of the tooth-size parameters ξ and σ on the zero-lift planar wing performances, as well as the influence of the investigated parameters on the lifting performance of incident wings that were obtained in the presented numerical investigations. These tendencies are described in detail above and, therefore, the corresponding experimental results are not discussed here any further.

7.0 RESULTS FOR LOCALLY SWEPT LATTICE WINGS

7.1 Results of the numerical investigations of LSLW

The selection of the numerically investigated lattice wing configurations was strongly limited because of the complexity of the geometry generation for numerical calculations. Two main types of novel lattice wings (*peak*- and *valley*-type) were investigated additionally to a comparable reference wing (Figure 18). The definition of the used names and parameters for the locally swept lattice wings are described in detail in chapter 3.2. One important simplification of the numerical models was the neglect of the outer framework influence, so that only cut-out segments from grid fins of infinite height h and span s were investigated numerically. The assignment of the tooth size to the cell size was fixed for these preliminary investigations with exactly one tooth per cell ($n_c = 1$). The thickness t and the nominal chord c_{nom} of each member in the lattice construction were selected similarly to the investigated locally swept planar wings with c_{nom} = 10mm, t = 0.5mm. Further simplifications in the numerical calculations, like inviscid wall conditions on the solid surfaces etc., are common with the calculations of planar wings.

a. **b.** **c.**

Figure 18: Numerically investigated lattice wing configurations: unswept wing $RLW_{10°}$(a), valley-type $LSLW_{v\_10°\_55°\_0.714}$ (b) and peak-type $LSLW_{p\_10°\_55°\_0.714}$ (c). The main grid fin parameters are c_{nom} = 10mm, t = 0.5mm, n_c = 1, $s \to \infty$, $h \to \infty$.

Results of numerical calculations of wing performance are presented in the following part. Figure 19 shows the wall pressure distribution for the two typical member surfaces A and B in the cell of the conventional lattice wing $RLW_{10°}$ at Mach number 4 for $\alpha = 0°$ (a) and 10°(b). The position of the surfaces A and B inside of the wing cell is marked on the sketch on the right side. The view of the lattice wing cell in this sketch is shown in flow direction. The difference of presented pressure distributions to the ones described above for planar wings can be seen mainly in the corners between the surfaces A and B, where the bow shocks additionally are co-interacting. The existence of these regions with higher pressure levels on the nose surfaces of the lattice wing causes a somewhat higher wave drag compared with the simple planar wing of same wetted area. The flow conditions in the lattice cell at incidence to the flow direction (Figure 19b) lead to an additional compression in the upper corner (surface A) and to a flow expansion in the opposite bottom corner (surface B).

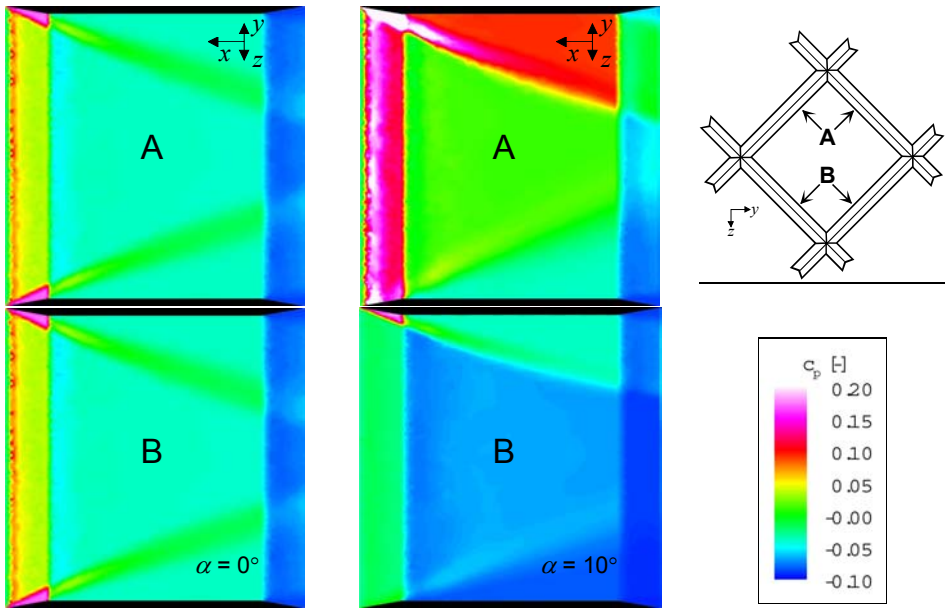

a. b.

Figure 19: Surface pressure distribution on two typical members A and B of an unswept grid fin $RLW_{10°}$ for $\alpha = 0°$ (a) and $\alpha = 10°$ (b) at $M_\infty = 4$.

The comparison of the surface pressure distributions at the corresponding side surfaces of the LSLWs (Figure 20) show that apart from the typical lower pressure levels at the nose part, which was already discussed on the planar wings, the two investigated lattice wing configurations are obviously different in the corner regions. The lattice wing configuration of the valley-type shows significantly higher pressure levels in these regions, as that of the peak-type. That is very remarkable and characterises the differences in the interactions of corresponding conical bow shocks in these cases. These two types of nodes have initially different orientations of the wave fronts near the interaction region, because the waves near swept obstacles are always oriented in sweep direction, and consequently, from “peak” to “valley”. So the interaction in the vicinity of the valley-type node is generated by two crossing compression shocks that have initial orientations to the opposite walls. Then again in the vicinity of the peek-type node the interaction is generated by two swept shock waves oriented from the peak. Consequently, the higher pressure in the first case can simply be explained.

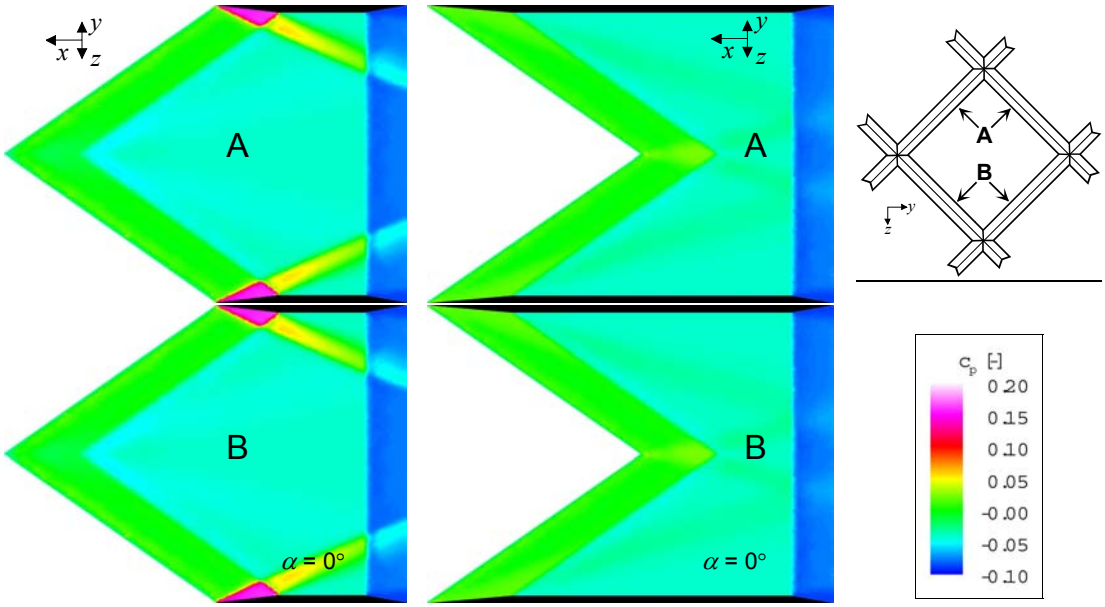

a. b.

Figure 20: Surface pressure distribution on two typical members A and B of grid fins from valley-type $LSLW_{v\_10°\_55°\_0.714}$ (a) and from peak-type $LSLW_{p\_10°\_55°\_0.714}$ (b) at $M_\infty = 4$ and $\alpha = 0°$.

The pressure distributions at α = 10° (Figure 21) show the development of this phenomena, where additionally some differences originate also on the upper and lower parts of the surfaces A under influence of the local yawed flow. From the comparison of both lattice wing types, on the first glimpse no advantages can be derived for one of the both however.

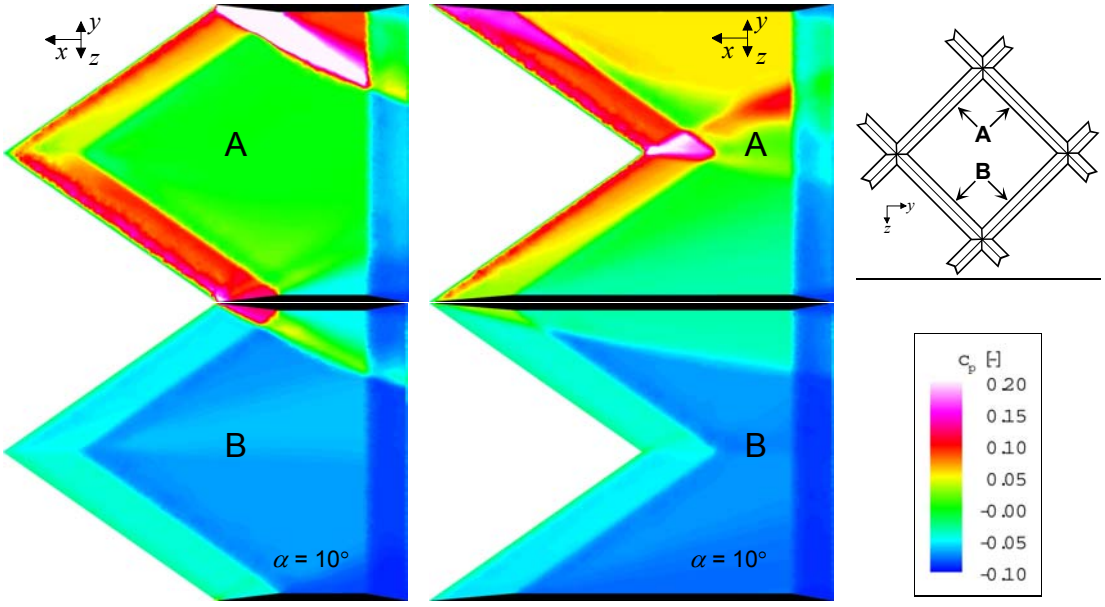

a. b.

Figure 21: Surface pressure distribution on two typical members A and B of grid fins from valley-type $LSLW_{v\_10°\_55°\_0.714}$ (a) and from peak-type $LSLW_{p\_10°\_55°\_0.714}$ (b) at $M_\infty = 4$ and $\alpha = 10°$.

The analysis of the Mach number distributions in different cross-sections A-E for the usual wing $RLW_{10°}$ (Figure 22) and the novel lattice wings from valley-type $LSLW_{v\_10°\_55°\_0.714}$ (Figure 23) and from peak-type $LSLW_{p\_10°\_55°\_0.714}$ (Figure 24) at free-stream Mach number $M_\infty = 4$ helps to complete the ideas over the different flow structures. In each of these figures the top sequences (sections A1-E1) presents the case without AoA, and the bottom sequences (sections A2-E2) the flow conditions a = 10°. The comparison of Mach number levels in the nose regions of the lattice wings (cross-sections A) indicates the positive effect of the leading edge sweep on the bow shock intensities – both investigated LSWL's have higher Mach number levels (weaker bow shocks) in this regions compared to the unswept lattice wing.

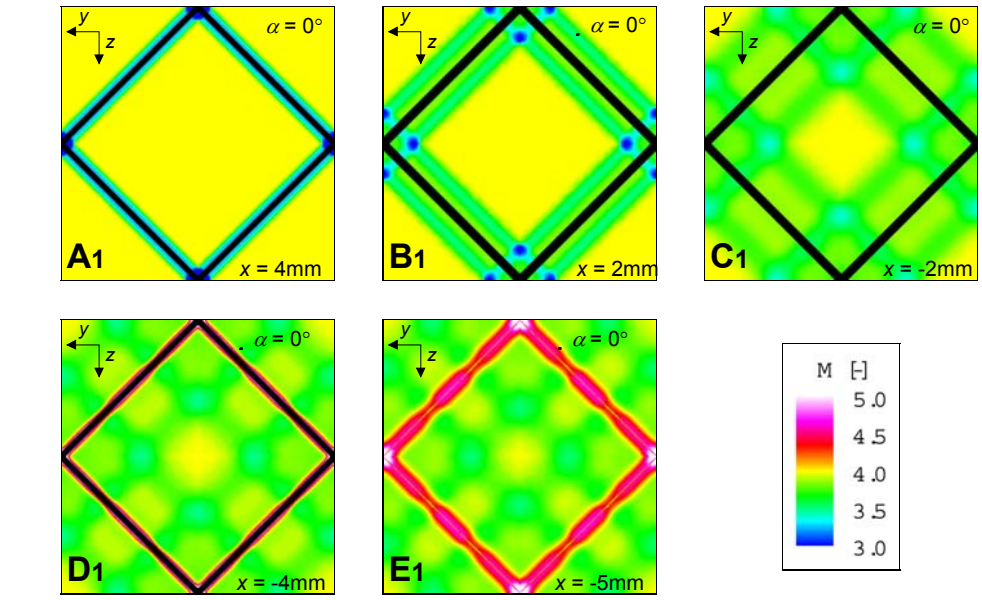

a.

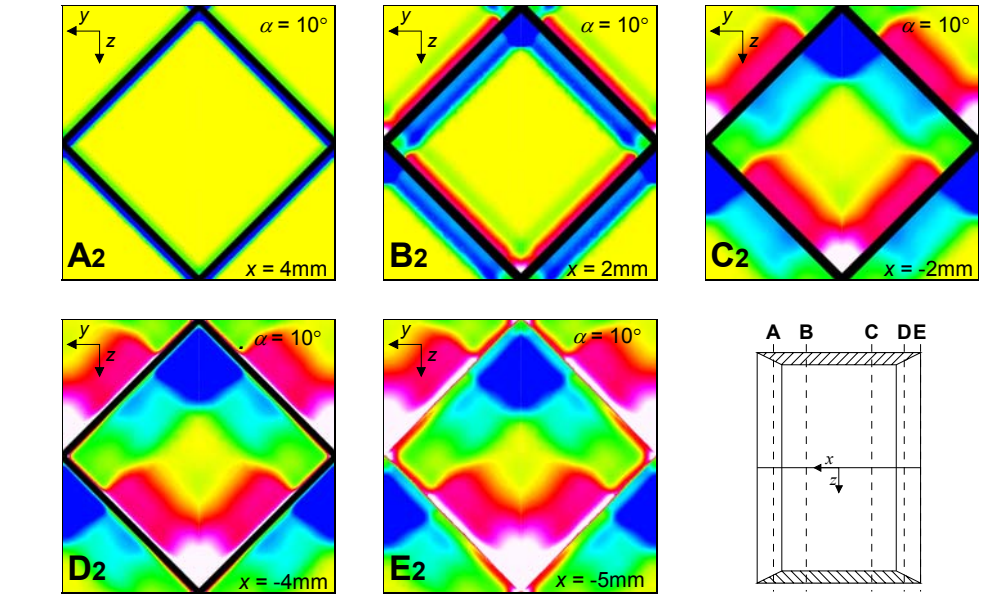

b.

Figure 22: Distribution of Mach number in a typical lattice wing cell of grid fins $RLW_{10°}$ for α = 0° (a, sections A1 - E1) and α = 10° (b, sections A2 - E2) at M_∞ = 4.

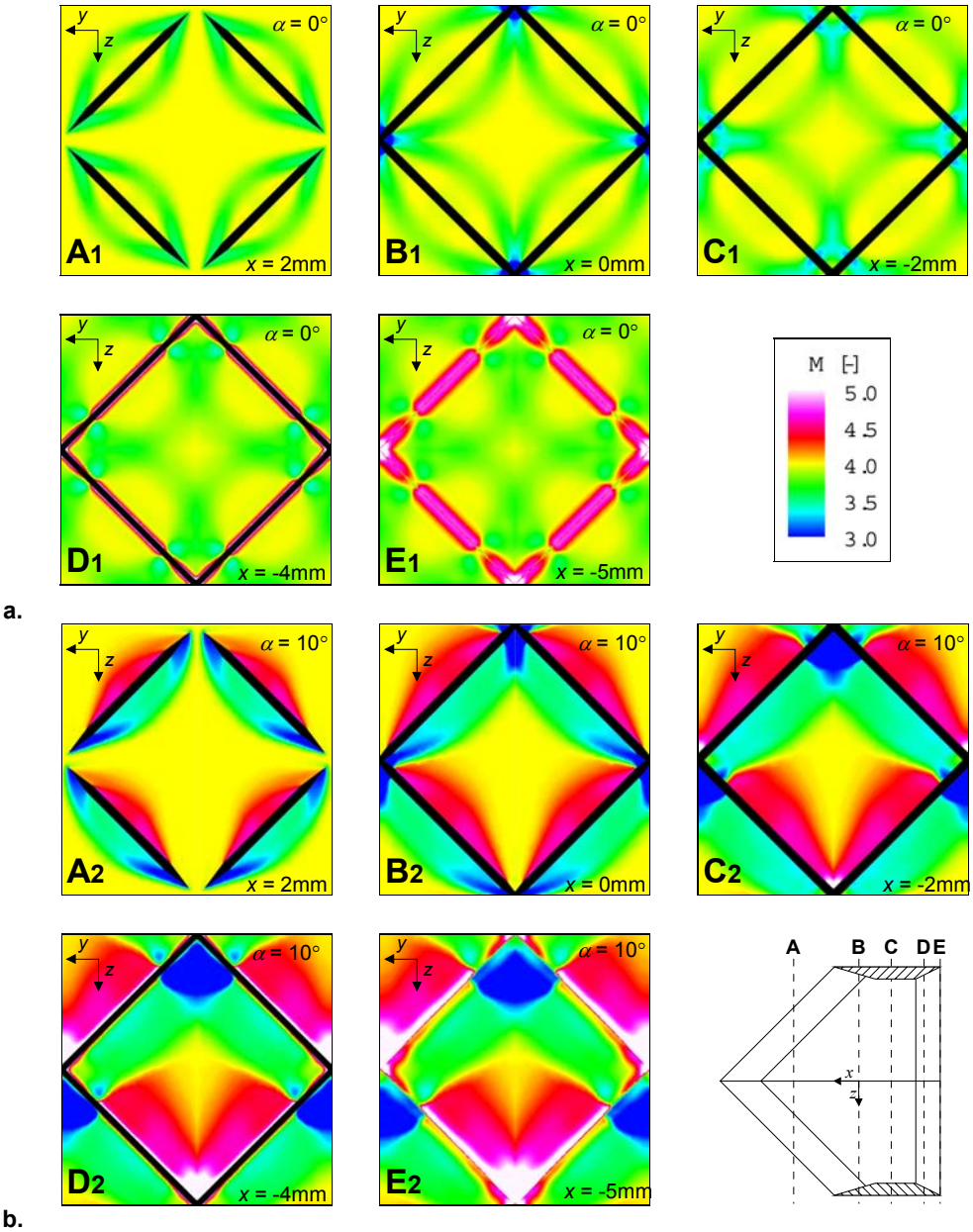

Figure 23: Distribution of Mach number in a typical lattice wing cell of grid from valley-type $LSLW_{v\_10°\_55°\_0.714}$ for $\alpha = 0°$ (a, sections A1 - E1) and $\alpha = 10°$ (b, sections A2 - E2) at $M_\infty = 4$.

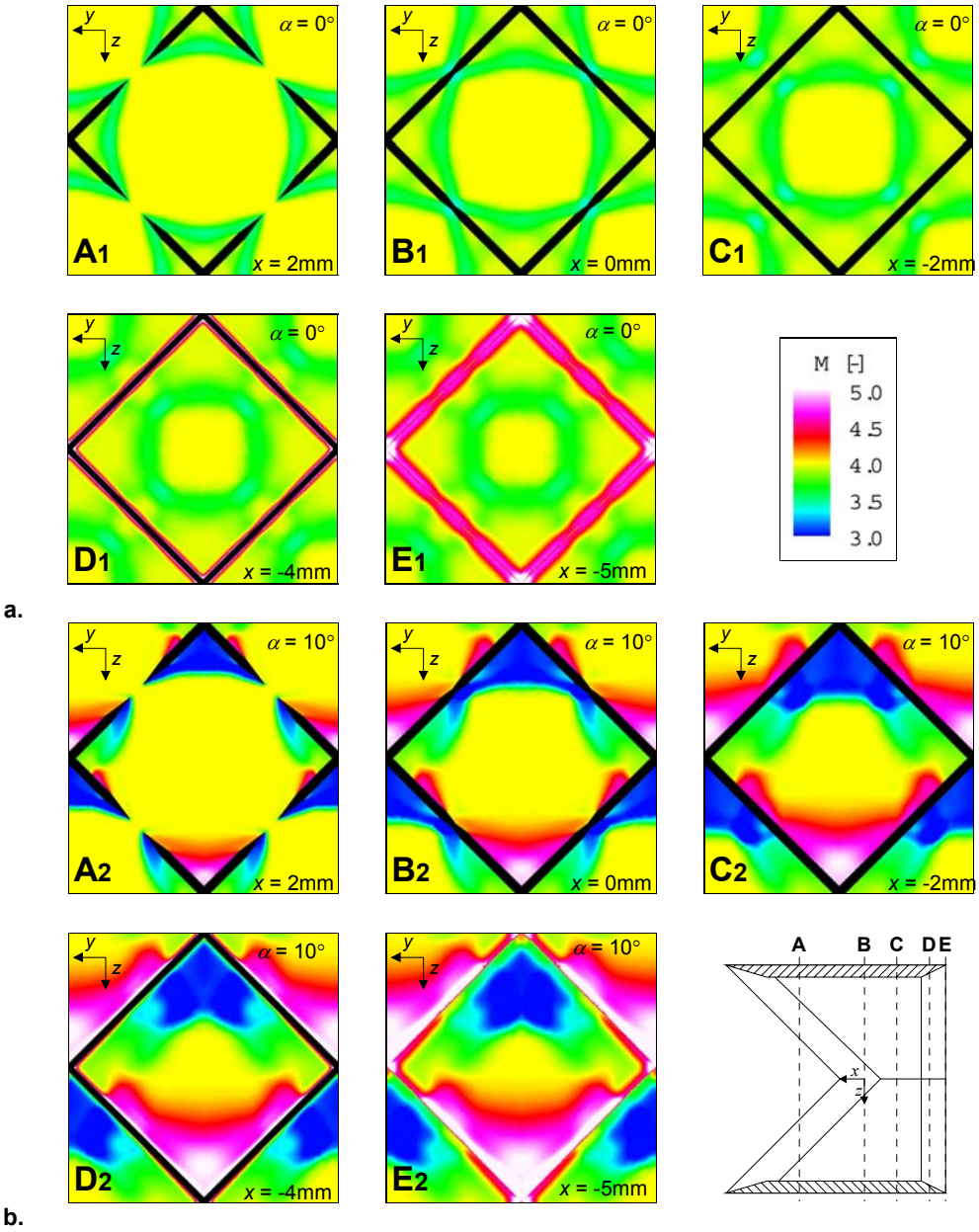

Figure 24: Distribution of Mach number in a typical lattice wing cell of grid from peak-type $LSLW_{p\_10°\_55°\_0.714}$ for $\alpha = 0°$ (a, sections A1 - E1) and $\alpha = 10°$ (b, sections A2 - E2) at $M_\infty = 4$.

The discussed regions of different surface pressure levels in the corners of both LSLWs due to the interaction of neighbouring bow shocks can be seen in the cross-sections B1. The relatively low Mach number in the corner regions of grid fins from valley-type (Figure 23, B1, blue areas) in opposite to the comparable zones in the case of a peak-type wing (Figure 24) demonstrates the higher intensities of the crossing shock waves in this regions. The prevailing shape of the wave structures and the complexity of its interactions within the cells for both lattice wing configurations can be derived from the observation of the presented Mach number distributions in the following cross-sections.

Figure 25 shows the effect of the leading edge sweep on the zero-lift wave drag (a) and on the zero-lift wave drag reduction (b) for the investigated Mach number range. The results confirm the expected trends in the Mach number. The determined profit in the wave drag lies between 32% and 42%. Furthermore, the

results show that according to zero-lift wave drag the wing of the peak-type is better than other LSLW. So at Mach number 6 the peak-type LSWL brings about 1.2% higher gains in the wave drag reduction. This effect has already been indicated and shortly analysed with the inspection of the surface pressure distributions.

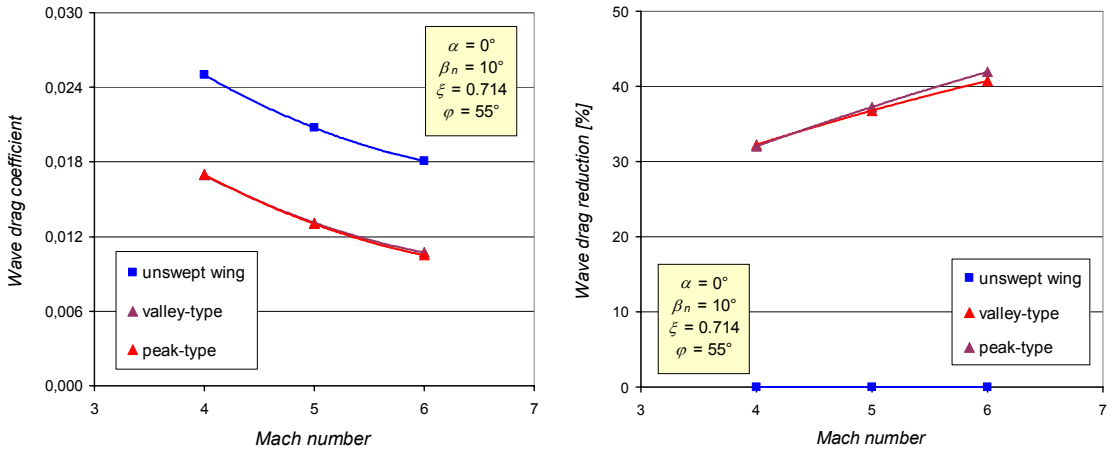

Figure 25: Effect of the local leading edge sweep on zero-lift wave drag coefficient (left) and on the relative wave drag reduction (right) vs. Mach number at $\alpha = 0°$ (unswept wing: $RLW_{10°}$, valley-type: $LSLW_{v\_10°\_55°\_0.714}$ and peak-type: $LSLW_{p\_10°\_55°\_0.714}$).

At wing incidence the profit in the lift-to-wave-drag ratio relative to ones of the unswept lattice wing (Figure 26) grows, as expected, with the Mach number. At $\alpha = 5°$ the profit reaches values between 25% and 37%. The locally swept wings show different characteristics. Furthermore, in opposite to the impression one gets from the zero-lift behaviour, the wing of the valley-type is suddenly more effective then one of the peak-type. So the additional gain in the lift-to-wave-drag improvement due to valley-type intersection of the member-planes lie between 1.7% and 5.3%, and even bigger for higher Mach numbers. These results are not unambiguous correlated with the described observations at $\alpha = 0°$ and therefore are somewhat unexpected. Responsible for this reversion in the effect of the favourable wing configuration is the enormous increase of the lift coefficient for the valley-type of the LSLW. So at incidence of 5 degree this wing shows about 8% higher lift coefficients as the rival. At $\alpha = 10°$ this gain increases to ~9%.

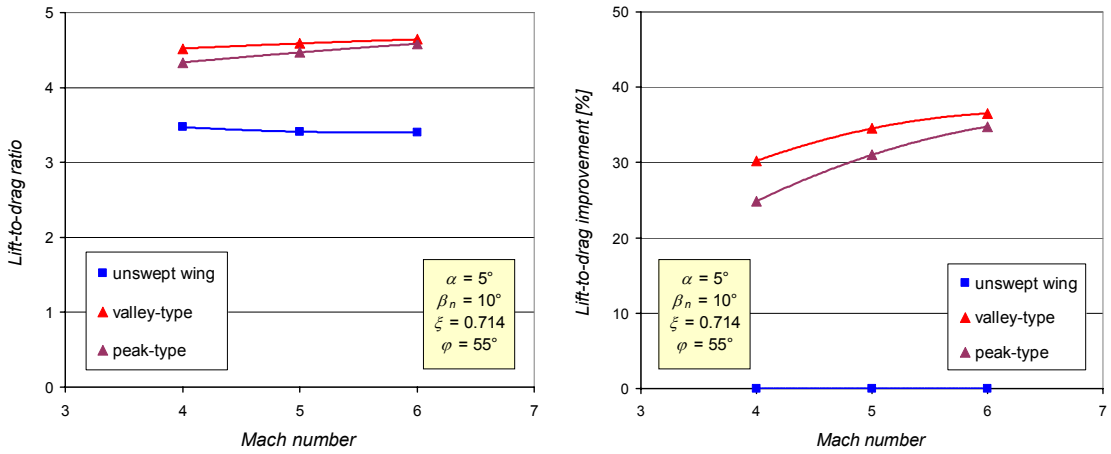

Figure 26: Effect of the local leading edge sweep on lift-to-wave-drag ratio (left) and on the lift-to-wave-drag improvement (right) vs. Mach number at $\alpha = 5°$ (unswept wing: $RLW_{10°}$, valley-type: $LSLW_{v\_10°\_55°\_0.714}$ and peak-type: $LSLW_{p\_10°\_55°\_0.714}$).

The reason for this increase of the lift coefficients is the mentioned region of the crossing shock's interaction near the upper corner of each cell (see Figure 21a, plane A), which provides very high surface pressure levels on the windward side of the lifting elements. Although the relative size of this region is not very large, it produces additional lift that is enough to improve the lifting characteristics of the valley-type of locally swept wing. This qualitative explanation is not checked by the integration of the surface pressures in different areas of the planes, but it seems to be the best one at the moment.

The direct comparison of the realistic wing performance obtained in wind tunnel tests gives additional information for the selection of the favourable lattice wing configuration from the examined pool. The results of such tests are presented in the next chapter.

7.2 Results of wind tunnel investigations of LSLW

This section presents the results of the wind tunnel measurements that were conducted on three real lattice wing models. These models include, similar to the numerical examinations, a reference unswept lattice wing and two locally swept configurations. The investigated configurations differ from the calculated ones. So was the half-angle of the sharpness β_n for technical reasons set to an angle of 17°. In the numerical investigations a value of 10° was used. Another difference is that both edges of the planes, therefore the leading and trailing edges, were locally swept. Furthermore, the framework of the lattice wing was also locally swept. Figure 27 shows photos of the examined lattice wings. In this case, to marks the "double" teeth rows, to the name of the wing was added a number "2". So, the double swept lattice wing of "peak2"-type get a name "p2", e.g. $LSLW_{p2\_17°\_55°\_0.714}$.

a. b. c.

Figure 27: Investigated lattice wing models for wind tunnel tests: a) unswept wing $RLW_{17°}$, b) double-valley-type $LSLW_{v2\_17°\_55°\_0.714}$ and c) double-peak-type $LSLW_{p2\_17°\_55°\_0.714}$.

The force measurements on the shown models were conducted in the Ludwieg Tube Facility RWG at three Mach numbers (M_∞ = 4, 5 and 6) and three angles of attack (α = 0°, 5° and 10°). Typical results for the effect of locally swept edges on the zero-lift total drag are presented in Figure 28. It is very impressive that the two tooth-wings clearly show a more favourable total drag in the investigated Mach number range. The effect is surely weaker then expected from the "friction-free" numerical calculations, but was reinforced due the higher values of the angle β_n. The obtained results show after all a reduction of the total drag between 32% and 38%. The tendencies of the Mach number effect confirm the numerical predictions. The presented experimental data show that the advantages of the peak-type configuration

opposite to the rival are just as predict. The gain in the total drag lies between 3% and 5%. It is possible that the reinforcement of this effect has emerged through the "double-tooth" edges.

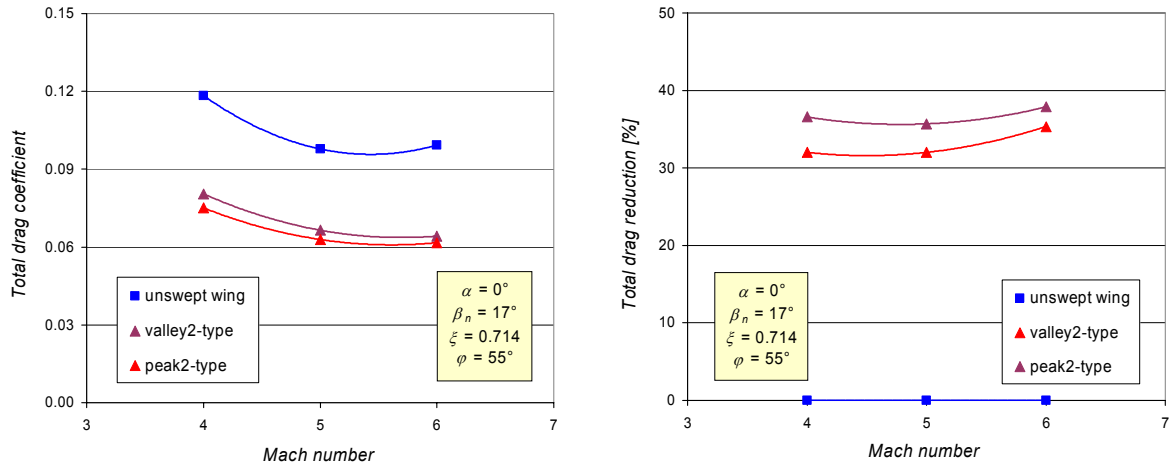

Figure 28: Influence of the locally leading edge sweeping on measured zero-lift total drag coefficient (left) and on the relative total drag reduction (right) vs. Mach number at $\alpha = 0°$ (unswept wing: $RLW_{17°}$, valley-type: $LSLW_{v2\_17°\_55°\_0.714}$ and peak-type: $LSLW_{p2\_17°\_55°\_0.714}$).

The lifting performance of the locally swept lattice wings is presented in Figure 29 on the example of results obtained at $\alpha = 5°$. Apart from mainly lower absolute values, compared with the calculated results from the lift-to-wave-drag ratio, the experimental results provide a full confirmation of the numerically predicted effects. So, the "valley2"-type wing shows the highest values of the lift-to-drag ratio in comparison to the unswept wing. The values in the profit for the "valley2"-type lie between 16% and 21% and for the "peak2"-type wing between 10% and 15%. Consequently, the advantages of the locally swept lattice wings have been confirmed in the present work not only numerically but also experimentally.

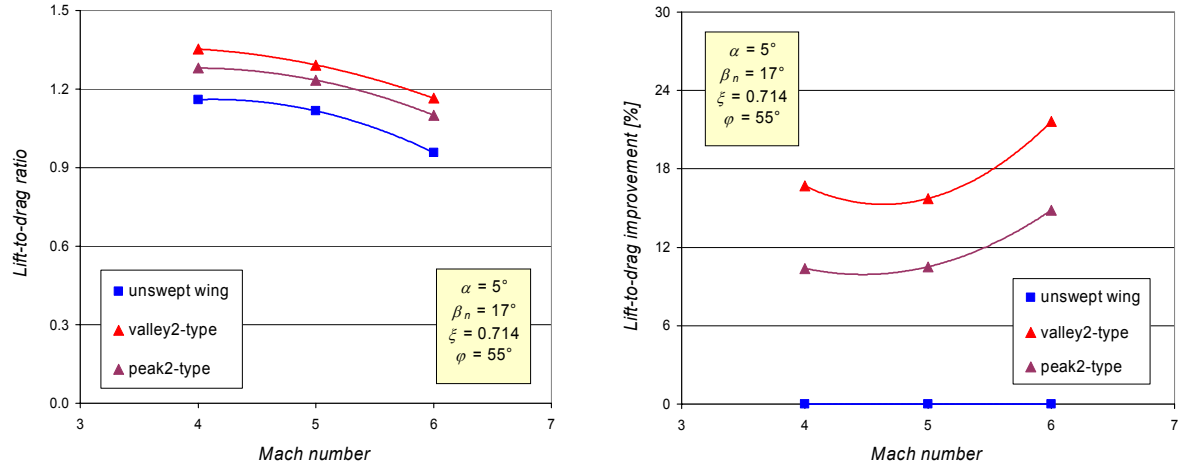

Figure 29: Influence of the locally leading edge sweeping on measured lift-to-drag ratio (left) and on the lift-to-drag improvement (right) vs. Mach number at $\alpha = 5°$ (unswept wing: $RLW_{17°}$, valley-type: $LSLW_{v2\_17°\_55°\_0.714}$ and peak-type: $LSLW_{p2\_17°\_55°\_0.714}$).

8.0 CONCLUSION

The high speed performances of novel locally swept lattice wing configurations were investigated. The examination includes numerical simulations of the supersonic flow around conventional unswept and

locally swept planar and lattice wings of infinite span as well as wind-tunnel tests on corresponding realistic finite span models in the Ludwieg Tube Facility at DLR (RWG). The investigations were performed at free-stream Mach numbers from 2 to 6 for angles of attack varied from 0 to 10 degrees.

The results show an essential reduction of the drag for the locally swept configurations. The most important results can be summarized as follows:

- The gained profit for the investigated realistic locally swept lattice wing configurations in comparison to the conventional ones in the zero-lift total drag amounts up to 38% and in the lift-to-drag ratio up to over 20%.

- The lowest zero-lift wave drag is shown by the lattice wing construction with the peak-type of locally swept lattice wings ($LSLW_p$ and $LSLW_{p2}$). On the contrary, better lift-to-drag performance at wing incidence is shown by the valley-type of LSLW ($LSLW_v$ and $LSLW_{v2}$).

- The effect of the LSE increases above all with the free stream Mach number, the local sweep angle, and the relative thickness of the members and the bluntness of their leading edges. It decreases with the incidence angle and for bigger relative tooth-sizes.

The experimental results were obtained on realistic lattice wings with a moderate sweep angles of 55° and with the half-angle of the leading edge sharpness of 17°, therefore the stated profits correspond to the total drag and the lift-to-drag ratio of this concrete configuration. According to the obtained tendencies these profits can be varied. An optimised configuration can provide even better results.

9.0 LITERATURE

[1] Belotzerkovsky, S.M., Odnovol, L.A., Safin, Yu.Z., Tyulenev, A.I., Frolov, V.P., Shitov, V.A., “Reschetchatye Kryl’ya”, Moscow, “Mashinostroeniye”, 1985 (in Russian); see also: Belotzerkovsky, S.M. et al., “Wings with internal Framework,” Machine Translation, FTD-ID(RS)T-1289-89, Foreign Technology Div., 1987.

[2] Sokolovsky G.A. et al., “Rocket with Lattice Control Surfaces,” European Patent Specification, EP 0 829 424 B1, Priority 11.05.1996, April 2003.

[3] Simpson, G. M., and Sadler, A. J., “Lattice Controls: A Comparison with Conventional, Planar Fins,” RTO MP 5, Proceedings of RTO AVT Symposium on Missile Aerodynamics, Sorrento, Italy, 1998, pp. 9.1–9.11.

[4] Washington, W. D., and Miller, M. S., “Experimental Investigations of Grid Fin Aerodynamics: A Synopsis of Nine Wind Tunnel and Three Flight Tests,” RTO MP 5, Proceedings of RTO AVT Symposium on Missile Aerodynamics, Sorrento, Italy, 1998, pp. 10.1–10.13.

[5] Kretzschmar, R. W., and Burkhalter, J. E., “Aerodynamic Prediction Methodology for Grid Fins,” RTO MP 5, Proceedings of RTO AVT Symposium on Missile Aerodynamics, Sorrento, Italy, 1998, pp. 11.1–11.11.

[6] Khalid, M., Sun, Y., and Xu, H., “Computation of Flows past Grid Fin Missiles,” RTO MP 5, Proceedings of RTO AVT Symposium on Missile Aerodynamics, Sorrento, Italy, 1998, pp. 12.1–12.11.

[7] Scott, J.A., “Missile Grid Fins,” http://www.aerospaceweb.org/question/weapons/q0261.shtml, February 2006.

[8] Psolla-Bress, H., „Kraft- und Momentenmessungen am X-Gitterflügel im TWG," DLR Internal Report, DLR-IB 223-98A17, DLR Göttingen, 1998 (in German).

[9] Esch, E., „Kraftmessungen an Gitterleitwerken im Überschall," DLR Internal Report, DLR-IB 39113-99C11, DLR Cologne, 1999 (in German).

[10] Schülein, E., „Aerodynamisches Auslegungs- und Optimierungstool für isolierte Gitterflügel FastGRIDS," 11. STAB-Workshop, 04.-05.11.2003, DLR Göttingen, STAB Jahresbericht 2003, pp.66-67 (in German).

[11] Reynier, Ph., Schülein E., „Incorporation of an Actuator Disc for Lattice Wing Modelling in an Unstructured Navier-Stokes Solver," in Notes on Numerical Fluid Mechanics and Multidisciplinary Design, Volume 87, Springer-Verlag, Berlin Heidelberg 2004, pp.132-139.

[12] Reynier, Ph., Reisch, U., Longo, J.-M., Radespiel, R., "Flow prediction around a missile with lattice wings using the actuator disc concept," Aerospace Science and Technology, 8, 2004, S. 377-388

[13] Esch, H., „Aerodynamische Beiwerte der Längsbewegung eines Flugkörpers mit Gitterleitwerk im Überschall," DLR Internal Report, IB 39113-2000C34, DLR Cologne, 2000 (in German).

[14] Henckels, A., „Experimente an Flugkörpergesamtkonfigurationen mit Gitterflügeln," DLR Internal Report, DLR-IB 32418-2002C13, DLR Cologne, 2002 (in German).

[15] Reynier, Ph., Longo, J.-M., and Schülein E., „Simulation of Missiles with Grid Fins Using an Actuator Disk," Journal of Spacecraft and Rockets, Vol.43, No.1, Jan.-Feb.2006, pp. 84-91.

[16] Fournier E.Y., "Wind Tunnel Investigation of Grid Fin and Conventional Planar Control Surfaces," AIAA Paper 2001-0256, 39st Aerospace Sciences Meeting & Exhibit, Jan. 8-11, Reno, NV, 2001.

[17] Washington, W. D., and Miller, M. S., "An Experimental Investigation of Grid Fin Drag Reduction Techniques," AIAA Paper 93-0035, Jan. 1993.

[18] Bushnell, D., "Supersonic Aircraft Drag Reduction," AIAA Paper 90-1596, AIAA 21st Fluid Dynamics, Plasma Dynamics and Laser Conference, Seattle, USA, 18.-20. June 1990

[19] Ludwieg, H., „Verbesserung der kritischen Machzahl von Tragflügeln durch Pfeilung," AVA – Bericht 45 H 07, 1945 (in German).

[20] Bertin, J.J., Smith, M.L., "Aerodynamics for Engineers," Prentice-Hall, Inc., 1979.

[21] Washington W.D., Booth P.F. and Miller M.S., „Curvature and Leading Edge Sweep Back Effect on Grid Fin Aerodynamic Characteristics," AIAA-93-3480-CP, AIAA Applied Aerodynamics Conference, August 9-11, 1993.

[22] Schülein, E., „Gitterflügel," German patent application, DE 10 2004 026 625 A1, June 2004 (see also: European patent application, EP 1 602 575 A2, May 2005) (in German).

[23] Guyot, D., „Experimentelle und numerische Untersuchung zum Einfluss der Lamellengeometrie auf die Leistung eines Hochgeschwindigkeitsgitterflügels," Diploma thesis, TU Berlin, February 2005 (in German).

[24] Gerhold, T., Friedrich, O., Evans, J., and Galle, M., "Calculation of Complex Three Dimensional Configurations Employing the DLR TAU Code," AIAA Paper 97-0167, Jan. 1997.

[25] Ludwieg, H., Hottner, Th., Grauer-Carstensen, H., „Der Rohrwindkanal der Aerodynamischen Versuchsanstalt Göttingen," Jahrbuch der DGLR 1969, S. 52 – 58, 1970 (in German).

[26] Ludwieg, H., „Der Rohrwindkanal," Zeitschrift für Flugwissenschaften ZFW, Vol. 3, Nr. 7, S. 206 – 216, 1955 (in German).

This page has been deliberately left blank

Page intentionnellement blanche